Journal of
Synchrotron Radiation

ISSN 0909-0495

Received 26 September 2011
Accepted 2 February 2012

Energy resolution of the CdTe-XPAD detector: calibration and potential for Laue diffraction measurements on protein crystals

Kadda Medjoubi,[a]* Andrew Thompson,[a]* Jean-François Bérar,[b] Jean-Claude Clemens,[c] Pierre Delpierre,[c] Paulo Da Silva,[a] Bernard Dinkespiler,[c] Roger Fourme,[a] Patrick Gourhant,[a] Beatriz Guimaraes,[a] Stéphanie Hustache,[a] Mourad Idir,[d] Jean-Paul Itié,[a] Pierre Legrand,[a] Claude Menneglier,[a] Pascal Mercere,[a] Frederic Picca[a] and Jean-Pierre Samama[a]

[a]Synchrotron Soleil, BP 48, Saint-Aubin, Gif sur Yvette 91192, France, [b]CNRS, Institut Neel, 25 Avenue des Martyrs, Grenoble 38042, France, [c]CPPM, Aix-Marseille Université and CNRS/IN2P3, 163 avenue de Luminy, 13288 Marseille, France, and [d]Brookhaven National Laboratory, Upton, NY 11973-5000, USA. E-mail: kadda.medjoubi@synchrotron-soleil.fr, andrew.thompson@synchrotron-soleil.fr

The XPAD3S-CdTe, a CdTe photon-counting pixel array detector, has been used to measure the energy and the intensity of the white-beam diffraction from a lysozyme crystal. A method was developed to calibrate the detector in terms of energy, allowing incident photon energy measurement to high resolution (approximately 140 eV), opening up new possibilities in energy-resolved X-ray diffraction. In order to demonstrate this, Laue diffraction experiments were performed on the bending-magnet beamline METROLOGIE at Synchrotron SOLEIL. The X-ray energy spectra of diffracted spots were deduced from the indexed Laue patterns collected with an imaging-plate detector and then measured with both the XPAD3S-CdTe and the XPAD3S-Si, a silicon photon-counting pixel array detector. The predicted and measured energy of selected diffraction spots are in good agreement, demonstrating the reliability of the calibration method. These results open up the way to direct unit-cell parameter determination and the measurement of high-quality Laue data even at low resolution. Based on the success of these measurements, potential applications in X-ray diffraction opened up by this type of technology are discussed.

Keywords: protein crystallography; Laue diffraction; CdTe pixel detector; energy resolution.

1. Introduction

The high flux, collimation and variable energy of X-rays produced by modern synchrotron radiation sources place huge demands on area detector technology. These demands have mainly been met by various types of integrating detectors, which are able to support the high global and local X-ray count rates coming from diffraction experiments at synchrotron sources. Single-photon-counting detectors, with all their advantages in signal-to-noise performance, have, with the exception of multiwire proportional chambers, found their use as 0D detectors for spectroscopic measurements. This situation is now changing rapidly, and a new generation of pixel array detectors (PADs, where each pixel is an individual photon-counting detector and consequently allows high local and global count rates) are opening up the possibility of new or improved types of measurements (for example, area detectors gated to fast external events, the use of the energy resolution of a detector to eliminate noise or measure in specific energy ranges). For a discussion of PADs, their operation and several typical applications see, for example, Henrich *et al.* (2009), Delpierre *et al.* (2007) or Rossi *et al.* (1999).

The potential of these PADs for synchrotron experiments is still under investigation, especially in terms of their energy resolution capabilities. In contrast to integrating detectors such as CCDs or imaging plates, photon-counting detectors can measure the energy spectrum of incident photons in addition to counting them. One way in which this energy information can bring a significant added value is for white-

beam (or Laue) diffraction experiments using synchrotron radiation.

The Laue method, described by Friedrich *et al.* (1912), and more recently 'rediscovered' for rapid time-resolved experiments in macromolecular crystallography (MX) (Helliwell *et al.*, 1989), consists of measuring the diffraction pattern obtained by exposing a stationary single crystal to a polychromatic ('white') X-ray beam. Diffraction spots from the crystal correspond to values of X-ray wavelengths selected by the sample that satisfy Bragg's equation $2d\sin\theta = n\lambda$. Different degrees of polychromaticity of the incident beam used for MX have been advocated, from the wide-energy-bandpass white-beam measurement (typically 0.5–2 Å) to the undulator-based 'pink beam' approach (Moffat, 1997), the choice of bandpass determining the overall flux available that can be chosen to match, as far as possible, the required temporal resolution of the experiment. A discussion of the choice of the bandpass of the X-ray source for Laue measurements is given by Šrajer *et al.* (2000). For given values of d and θ the Bragg equation is satisfied by ($n = 1, 2, \ldots$ and λ, $\lambda/2, \ldots$). Accordingly, a certain number of reflections superpose completely in the measured diffraction pattern. Most reflections correspond to a single wavelength (singlet) and the number of 'wavelength overlapped' reflections (multiplets) varies as a function of the diffracted resolution range of the crystal, the crystal orientation with respect to the X-ray beam, and the energy bandpass of the incident beam. In the worst case, about 16% of all reflections can be energy multiplets (Cruickshank *et al.*, 1987) and, even at a typical diffraction resolution, 10% of spots can be energy multiplets. Reflections measured at low $\sin\theta/\lambda$ are those most likely to be multiplets, and the fact that they are not easily measurable causes a lack of completeness of data at low resolution, often referred to as a 'low-resolution hole'. This situation is difficult to recover experimentally unless the symmetry of the crystal and multiple measurements allow their collection 'non-overlapped' at a different crystal orientation. This latter approach is not always possible or even advisable as radiation damage by the white beam is a very severe constraint. The effect of energy overlaps is then to give systematically incomplete data at low resolution, which in turn gives rise to electron density maps with marked discontinuities and that are often difficult to interpret. A number of statistical approaches exist for the deconvolution of these energy-overlapped intensities (Hao *et al.*, 1995; Bourenkov *et al.*, 1996; Ren & Moffat, 1995), all of which enjoy a reasonable degree of success. Direct measurement of the different energy components was possible with non-energy-resolving detectors by introducing absorbing foils either between X-ray-sensitive films (Helliwell *et al.*, 1989) or in front of a non-energy-dispersive detector on a specialized goniometer (Hanley *et al.*, 1997). Several experimental approaches, using different types of detector, are being developed in order to measure these reflections, and can be found in the recent literature (Send *et al.*, 2009; Toyokawa *et al.*, 2010). Here we describe the energy calibration of the XPAD3S detector and its application for measuring and indexing multiplet reflections from a hen egg-white lysozyme crystal.

2. The XPAD3 detector

2.1. Detector description

The XPAD, a hybrid pixel detector, is developed within the framework of the XPIX collaboration (SOLEIL, Institut Néel/CNRS and Centre de Physique des Particules de Marseille/CNRS). It consists of a fully depleted sensor bump-bonded, by using flip-chip technology, to a readout circuit, the XPAD3S (Pangaud *et al.*, 2007). The circuit, designed in the 0.25 µm IBM technology with a radiation-hard process, is composed of 9600 pixels (120 lines × 80 columns). The pixel size is 130 µm and the total active area is then about 1.5 cm × 1.0 cm. Each pixel contains a complete electronic photon-counting readout chain with a single threshold energy selection.

The front-end is composed of a low-noise charge-sensitive amplifier (CSA) followed by an operational transconductance amplifier (OTA). As the XPAD3S was designed for use with a sensor working in hole collection mode, the CSA input polarity is positive. The sensitivity and the equivalent noise charge (ENC) (Radeka, 1988) of the front-end have been evaluated in previous work (Pangaud *et al.*, 2008) and are, respectively, 320 pA electron^{-1} and about 130 electrons r.m.s. Depending on the sensor used and according to the electron–hole pair creation energy (Spieler, 2008), the ENC corresponds to 470 eV for Si and 575 eV for CdTe.

With the shaping time typically used for this chip, the deadtime of the front-end, which roughly corresponds to the width of the output pulse at the threshold level (Bergamaschi *et al.*, 2010), is 400 ns. As the counting chain is based on a paralyzable counter, the output counting rate is linear at the 5% level up to a few 10^5 photons s^{-1} pixel^{-1}.

A global threshold (known as ITH) is used for energy discrimination. Owing to the differences in characteristics between pixels (sensitivity and offset at the output of the front-end, differences in comparators, *etc.*) the effective threshold value varies from pixel to pixel. This dispersion is corrected by using a local threshold correction (known as DACL) implemented on each pixel. ITH and DACL are using, respectively, 8- and 6-bit DACs. A further 8-bit DAC, called ITUNE, sets the weight of the lowest significant bit (LSB) of DACL and also ITH, *i.e.* the global threshold step. In the first version of the chip, the XPAD3S.1, a larger than expected pixel-to-pixel threshold dispersion was measured. A variation of the offset at the OTA output from the left to the right of the circuit was observed, and can be explained by a non-uniform distribution of the bias voltage to the pixels' analog chain (Chantepie, 2008). In order to correct for this effect, the whole DACL dynamic range and a larger threshold step are used. In consequence, the lowest usable step ITH is 0.7 keV for Si and 1 keV for CdTe.

When a signal higher than the threshold is detected, the output signal from the discriminator increments a 12-bit counter with an overflow bit whose state is repetitively recorded by the DAQ (data acquisition) board. With this technique a dynamic range is attained that is only limited by the bit depth of the allocated memory on the DAQ board (27-bits in our case; Dawiec, 2011). Currently, the counters of all

pixels can be read out in 4 ms before starting a new image acquisition (Dawiec, 2011). However, in the first version of the chip the readout 'on the fly' of the overflow bit induces noise events, at least for low ITH. As a consequence it was decided to disable the counters for 100 µs during the overflow bit readout.

A second version of the chip, the XPAD3.2S, has been developed in order to correct the effect of the excess of dispersion, and hence to reduce the threshold step and to allow overflow bit readout on the fly. At the same time, the new circuit was improved for pump–probe experiments in order that all counters of the chip can be simultaneously externally triggered with gates of duration down to 100 ns. The XPAD3.2S is currently under characterization and has already demonstrated good performance for these pump–probe applications (Medjoubi *et al.*, 2011).

Two XPAD detectors have been used for the Laue energy-resolved experiment described in this article: an XPAD3S-Si module and a quad XPAD3S-CdTe. The two detectors are shown in Fig. 1. These types of detectors have been fully characterized in terms of imaging and detection performances and the results are described by Medjoubi *et al.* (2010).

The XPAD3S-Si consists of a 1.5 cm × 7 cm monolithic silicon sensor of 500 µm thickness bump-bonded to seven XPAD3.1S chips placed side by side. The sensor is an array of 120 × 560 pn junctions made of a high-resistivity (6000 Ω cm) n-type silicon bulk. The back side, which is in front of the chips, is pixelated with p+ doped implants that are aluminized. The pads are squares of 100 µm side and spaced by 130 µm in both directions. The front side is an ohmic contact. This sensor, designed for hole collection, is biased at 150 V in order to be fully depleted.

The XPAD3S-CdTe consists of two 2 cm × 1.5 cm monolithic CdTe sensors of 750 µm thickness, from Acrorad (http://www.acrorad.co.jp/), hybridized on 2 × 2 XPAD3.1S circuits, and hence covering a sensitive area of 2 cm × 3 cm. The sensor is an array of 160 × 120 Schottky diodes made of a high-resistivity p-type CdTe bulk. The pixel arrangement is identical to that for the silicon sensor. Pad contacts are made with 200 nm of Pt (ohmic contact), and the Schottky barrier, on the front side, consists of an indium–titanium multilayer contact. This structure allows use of the sensor in hole collection mode for compatibility with the circuit input polarity. Previous studies have shown than a 900 V reverse bias is necessary to obtain a high charge collection efficiency (CCE) (Basolo *et al.*, 2008).

(*a*) (*b*)

Figure 1
(*a*) XPAD3S-Si module. (*b*) Quad XPAD3S-CdTe.

As expected with Schottky contacts, a polarization phenomenon (Toyama *et al.*, 2006) is observed. This effect gradually degrades the CCE during X-ray illumination. As demonstrated by Basolo *et al.* (2008), a sequence of switching off and on the bias voltage after data collection is used to restore the initial value of the CCE.

The readout architecture of the XPAD3 detector used for this experiment is divided into three blocks: the XPAD3 detector, a USB-opto board and a TANGO (http://www.tango-controls.org/) device control and acquisition system running on a computer. The readout and the control of the chip are performed by an electronic board, the CYCLONE board, on which an FPGA (field programmable gate array) CYCLONE II chip (Altera Corporation, San Jose, CA, USA) contains an embedded processor (NIOS II). Data from the CYCLONE board are sent to the USB-opto board, and hence to the controlling computer, *via* an optical fiber.

The TANGO device can send configuration parameters (ITH, DACL, ITUNE, *etc.*) to the detector, define the exposure time, start the acquisition and download the image. In this experiment, commands and attributes of the TANGO device were called by MATLAB (The MathWorks, Natick, MA, USA) functions *via* a TANGO binding. MATLAB scripts have been written for the calibration and for specific acquisitions as presented in this paper.

2.2. Detector calibration

For a single-photon-counting two-dimensional pixel detector, image quality factors that are quantified by the modulation transfer function (MTF) and the detective quantum efficiency (DQE) are strongly influenced by the threshold uniformity across all pixels and energy calibration. As an example, an energy threshold below half of the incoming energy photon will enlarge the spatial resolution (decreasing the MTF) (Marchal, 2010) and an uncorrected threshold dispersion will increase the fixed-pattern noise, thus reducing the DQE. Therefore adjustment of local and global thresholds is necessary in order to obtain an optimal image quality at a specific energy, the procedure being described in §2.2.1.

An important advantage of this type of detector is its ability to measure the energy spectrum of incident photons. With the XPAD detector, this spectrum can be obtained by differentiation of the so-called S-curve, *i.e.* the counting rate as a function of the threshold. This curve is obtained for all pixels by taking images at various thresholds. The quality of this measurement depends on the threshold energy calibration, the threshold step and the threshold uniformity across the detector. Therefore it is essential to correct as much as possible the intrinsic non-uniformity caused by threshold

dispersion between pixels. The procedures used by the authors for setting both local and global thresholds are described in §2.2.2.

2.2.1. Threshold-setting procedure. As stated above, the local correction per pixel (DACL) associated with the global threshold (ITH) per circuit corrects pixel-to-pixel energy dispersion. Thus a set of DACL and ITH values have to be defined for all required energy threshold values, and loaded into the detector when the operating energy is changed. To determine a set of threshold values, the detector is exposed to a uniform irradiation (flat field) at the required energy. With the DACL of all pixels set at the middle of its range (*i.e.* 32), images are recorded while increasing the global threshold (ITH) value. For each circuit a starting optimal global threshold is obtained when almost half of the pixels are counting photons. Once this global threshold is established, a DACL scan over the whole 6-bit range is performed for each individual pixel. The inflection point of each S-curve thus obtained corresponds to the required threshold adjustment per pixel at the target energy. These curves are evaluated by fitting the S-curve with an analytical function which corresponds to the integration of the theoretical energy response of a photon-counting pixel detector. The detector energy response, R, for a given incident photon energy, E_0, can be described by a simplified model which is written as follows (Ponchut, 2008),

$$R(E, E_0) = (1 - k)n_{\rm p}(E, E_0) + kn_{\rm cs}(E, E_0), \qquad (1)$$

where k is the charge-sharing probability, $n_{\rm p}$ the photo-peak distribution and $n_{\rm cs}$ the charge-sharing distribution. $n_{\rm p}$ is assumed to be described by a Gaussian function with standard-deviation ENC, and $n_{\rm cs}$ by a Heaviside function. Both functions are normalized by their integrals.

The S-curve along the energy threshold ($E_{\rm T}$) can be modelled by the integration from $E_{\rm T}$ to infinity of the energy detector response function multiplied by the total number of detected events ($N_{\rm T}$). The function is presented below,

$$S(E_{\rm T}) = N_{\rm T}\left\{ -(k/E_0)(E_{\rm T} - E_0)\,\text{Heaviside}(E_0 - E_{\rm T}) + (1 - k)\left[1 - \text{erf}\left(\frac{E_{\rm T} - E_0}{2^{1/2}\,\text{ENC}}\right)\right]\right\}, \qquad (2)$$

with erf being the error function.

S-curves are fitted with function (2) (E and E_0 being replaced by DACL and DACL_0) by using the curve-fitting MATLAB toolbox. Inflection points (DACL_0) are extracted, converted to the nearest integers and uploaded to the chip.

This integer DACL_0 value distribution must be centred within the DACL dynamic range in order to minimize the number of uncorrectable pixels outside the DACL range. Hence, if the distribution is not centred, the ITH value is modified and the sequence is repeated until this condition is fulfilled.

Fig. 2 presents a DACL_0 distribution, obtained in this manner, for one chip of the XPAD3S-CdTe detector with

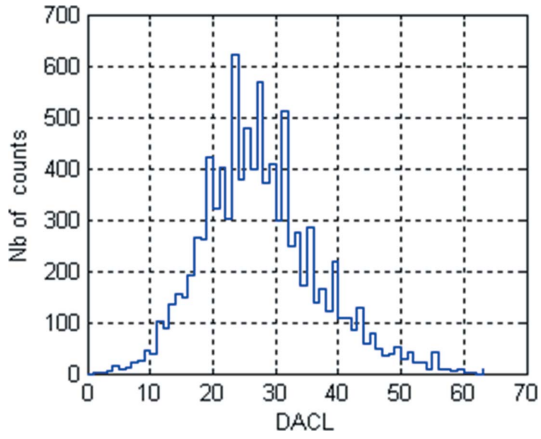

Figure 2
Intrinsic local threshold dispersion of one chip of the XPAD3S-CdTe at 10 keV.

illumination at 10 keV. This distribution corresponds to the intrinsic pixel threshold dispersion across the chip and, as detailed in §2.1, owing to the left–right offset variation, the distribution covers the entire dynamic of the DACL value. This problem is corrected in the second version of the XPAD3S.

DACL_0 and ITH_0 values found in this way are then uploaded to the detector so that all pixel thresholds are set at 10 keV. The setting error is given by the residual threshold dispersion that is caused by DACL quantization errors and the inaccuracy determination of the inflection points. This dispersion is evaluated by exposing the detector to a 10 keV flat field and scanning the global threshold ITH. The S-curves are then fitted with function (2) (where E and E_0 are replaced by ITH and ITH_0), leading to the determination of the inflection point ITH_0 per pixel. Fig. 3 shows the ITH_0 distribution on one chip. The residual dispersion given by the standard deviation of the distribution presented in Fig. 3 is 0.47 step of ITH, which corresponds to 470 eV for the CdTe sensor.

For energy-resolved experiments, this threshold dispersion correction procedure has to be carried out for all useful

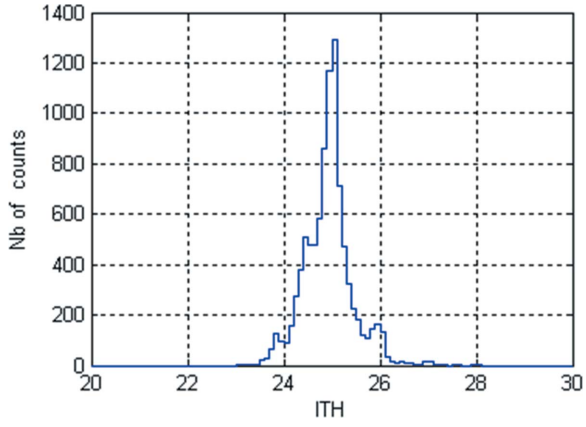

Figure 3
Global threshold distribution after DACL uploading on one chip of the XPAD3S-CdTe at 10 keV.

energies. This makes the method time-consuming (long process, long upload, long iteration) and difficult to implement (flat field required for each energy). Furthermore, the energy resolution that can be achieved cannot be lower than the residual dispersion determined above, *i.e.* 470 eV.

2.2.2. Threshold setting procedure for energy-resolved experiment. Thresholds setting were established using the above procedure at the minimum energy to be used in the measurement, 10 keV in our case. This was followed by the calibration of energy *versus* global threshold for each pixel. This calibration was obtained from the ITH scans measured at 15, 20, 25 and 30 keV. The four S-curves per pixel thus obtained were then adjusted using function (2) (*cf.* Fig. 4) and hence four non-integer ITH values corresponding to the four inflection points were obtained per pixel.

As front-end and comparator responses are considered to be linear within the incident energy range, the ITH inflection point values against the corresponding energy were fitted with a linear function. To evaluate the performance of the method on the XPAD3S-CdTe a region of interest (ROI) of 400 pixels was defined. Within this ROI, the slope and the offset were extracted for each pixel, and distributions of both parameters were evaluated. The averaged slope value and its standard deviation were 1 keV/ITH and 0.13 keV/ITH, respectively. The averaged offset value and its standard deviation, which corresponds to the residual threshold dispersion, were 10.6 keV and 450 eV, respectively, which is roughly the same as obtained in §2.2.1.

The energy calibration of the global threshold allows us to correct, with the offset-per-pixel, the residual threshold dispersion and to correct, with the slope-per-pixel, the dispersions of the front-end sensitivity and the ITH LSB weight.

In order to evaluate the accuracy of the energy reconstruction using this procedure, the detector was exposed to air-scattered X-rays at 25, 25.1, 25.2, 25.3, 25.4, 25.5 and 26 keV. The threshold dispersion correction measured at 10 keV was uploaded and an ITH scan performed for each incident energy. The ITH scale of each S-curve per pixel is then converted to energy with the linear calibration per pixel detailed above. The S-curves of pixels contained in the ROI are adjusted with function (2) in order to estimate their inflection point. Fig. 5 presents the distributions of inflection points measured for each incident energy.

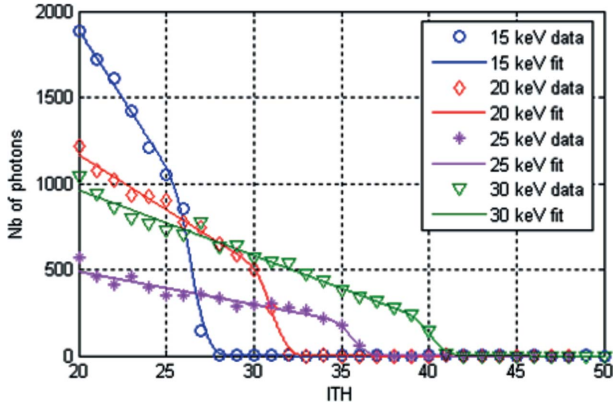

Figure 4
ITH scans (raw data and fit) on one pixel of the XPAD3S-CdTe for different incident X-ray energies.

Table 1
Average and standard deviation of the reconstructed incident energy distributions presented in Fig. 5.

	Energy (keV)						
	25	25.1	25.2	25.3	25.4	25.5	26
Average (keV)	25.03	25.12	25.19	25.31	25.42	25.53	26.04
Standard deviation (eV)	141	137	136	140	132	139	143

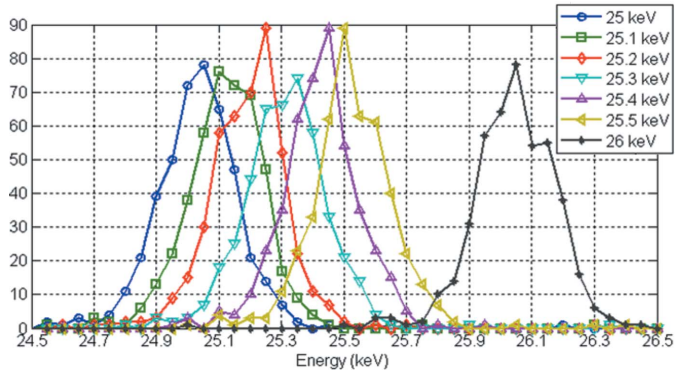

Figure 5
Energy distribution measured with the XPAD3S-CdTe for different incident photon energies.

The average value and standard deviation of each histogram are given in Table 1. As shown in the table, the incident photon energy can be reconstructed on each pixel with an accuracy of 140 eV. Therefore, this method gives an energy resolution that is well adapted to experiments such as energy-resolved Laue diffraction.

3. Laue experiment

3.1. Experimental configuration

The experiment was performed on the METROLOGIE beamline (Idir *et al.*, 2010) at Synchrotron SOLEIL. The beamline is installed on a bending-magnet source with two branches for hard and soft X-rays, respectively, giving a monochromatic beam covering an energy range from a few eV up to 40 keV. Laue measurements were performed on the hard X-ray branch line, but with the double-crystal monochromator vertically displaced to allow the 'white' bending-magnet spectrum to pass. In order to control the energy range of X-rays used for measurements, a grazing-incidence reflection from a 60 nm-thick Pt-coated plane silicon mirror was used to set the upper limit of the energy spectrum to approximately 45 keV, and a 200 µm-thick Al foil was used to attenuate radiation below 10 keV. This attenuator had the added function of protecting the protein crystal sample from the softer part of the X-ray spectrum, which gives less information per photon prior to radiation death of the sample. The calculated

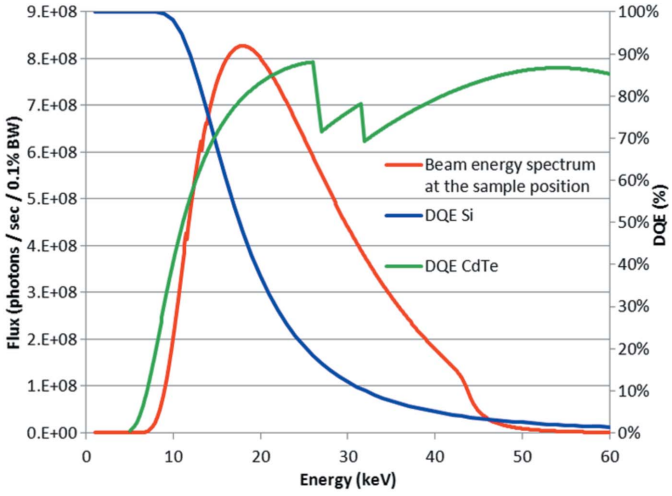

Figure 6
Beam energy spectrum calculated at the sample position for the SOLEIL storage ring (red curve). Blue and green curves show the calculated DQE of the XPAD3S-Si and XPAD3S-CdTe, respectively (Medjoubi *et al.*, 2010).

white-beam spectra reflected by the mirror are shown in Fig. 6 (using the software *XOP*; Sanchez del Rio & Dejus, 2004), and take into account the beam path to the sample (150 µm-thick CVD diamond windows and 1.30 m in air). Fig. 6 also shows the DQE of the XPAD3S-CdTe and XPAD3S-Si within the beam spectrum energy range. The presented DQE has been calculated according to a proven model described by Medjoubi *et al.* (2010).

A photograph of the experimental set-up is shown in Fig. 7. The experimental hutch is equipped with various positioning stages and ancillary equipment which allowed the crystal to be aligned on a vertical rotation axis.

A hen egg-white lysozyme (HEWL) crystal, cryo-protected in oil and kept at approximately 100 K by a stream of cold nitrogen gas (Oxford Cryosystems- Cryostream 600 series),

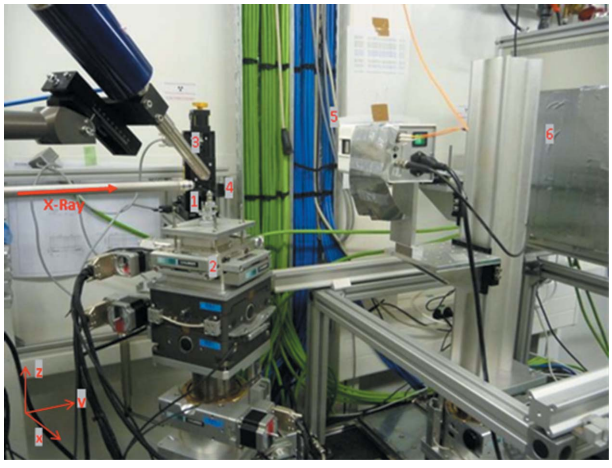

Figure 7
Photograph of the experimental set-up. The beam comes from the left. Main elements are numbered: (1) sample; (2) translation–rotation stage; (3) cryostream; (4) beamstop; (5) XPAD3S-CdTe (in position for acquisition); (6) the MAR345 protected by a lead screen and displaced from the acquisition position during the XPAD measurements.

was mounted on a vertical-axis rotation stage with *X*–*Y*–*Z* translation stages (*X*, horizontal; *Y*, along the beam direction; *Z*, vertical). An optical microscope system was used for crystal centring in the X-ray beam. The beam size was limited to 500 µm × 500 µm by slits. An X-ray shutter (Cedrat systems FPS-400m) was used to control the timing of sample exposures. The XPAD3-CdTe and XPAD3-Si detectors were interchangeably mounted on a *Y*–*Z* translation stage allowing a wider diffraction surface to be measured by translating the detector. Along the beam direction the detector could approach to within 150 mm of the crystal sample. A tungsten beamstop prevented the non-absorbed beam from hitting the detector surface. A MAR345 imaging-plate detector (MARresearch, Germany), mounted on a sliding stage, was used to record the full diffraction pattern from the crystal in order to simplify the task of indexing the diffraction pattern.

Tetragonal crystals of HEWL and orthorhombic crystals of thaumatin were produced using the hanging drop method and well known protocols described in the literature. Diffraction images were collected as follows:

(i) A series of still images separated by a rotation angle of 10° were collected using the MAR345 detector in order to determine the crystal orientation with respect to the X-ray beam and to acquire a high-completeness data set. Note that, owing to the composition of the image plates, this detector retains a high DQE even at fairly high energies, and is hence well matched to the energy spectrum chosen.

(ii) Large-area Laue diffraction patterns were collected by translating the XPAD using the *X*–*Z* stage, with 5 mm overlaps to enable the reconstruction of the whole image. This method of collecting data was severely limited owing to X-ray radiation damage of the crystal samples occurring between the acquisition of the first and last images, and the results are consequently not presented here.

(iii) In order to limit the radiation damage to the sample, only a small and easily identifiable part of the diffraction pattern, chosen at low Bragg angles in order to contain a number of multiplet reflections, was isolated using both the XPAD3S-CdTe and XPAD3S-Si detectors. Diffraction images were collected at a single sample orientation while incrementing the energy threshold (ITH) of the detector with the minimum usable step (as discussed in §2.1, 1 keV for the CdTe and 0.7 keV for the Si detector) between 10 keV and 45 keV for the CdTe detector, and 10 keV and 30 keV for the Si detector. In order to keep a sufficient signal-to-noise ratio, the exposure time (4 s) was linearly increased by 450 ms steps within the energy threshold range.

(iv) The X-ray shutter was closed both between energy steps and *X*–*Z* translation steps to avoid unnecessary exposure of the crystal to the beam.

3.2. Results

Laue diffraction images from a single HEWL crystal were recorded as described above, and the crystal orientation/indexing was determined from five diffraction images collected at 10° angular increments with the MAR345 detector

Table 2
Energy and multiplicity of the spots circled in Fig. 8.

Positions of indexed reflections on the detectors [(*a*) MAR345, (*b*) XPAD-Si, (*c*) XPAD-CdTe in Fig. 8] were extracted from the fitted integrated reflection file, as calculated with the program *LAUEGEN*. Their Miller indices and 2θ angle were used to calculate the expected E_0, and the expected multiplicity extracted from the *LAUEGEN* output. Equivalent reflections were visually identified on the XPAD-CdTe detector. The measured E_0 corresponds to the energy of the peak intensity pixel, and the observed multiplicity corresponds to the number of maxima in the differentiation of the energy fit (up to a maximum measured energy of 45 keV).

hkl	Expected E_0 (keV)	Measured E_0 (keV) with the XPAD3S-CdTe	Expected multiplicity in the experimental 10–45 keV energy range	Observed multiplicity
5 2 0	14.9	15.3	2	2
7 0 1	16.4	16.5	2	2
7 3 0	13.8	13.9	3	2
7 3 2	32.8	33.0	1	1
8 5 3	20.7	21.1	2	2
8 6 1	40.8	39.8	1	1
12 2 1	29.3	28.8	1	1
14 3 1	28.1	27.8	1	1

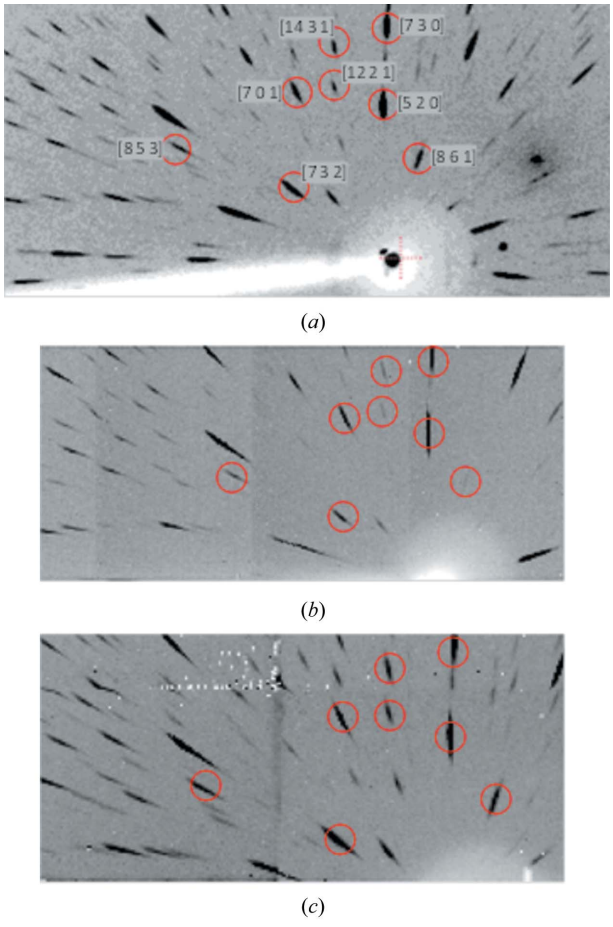

(*a*)

(*b*)

(*c*)

Figure 8
(*a*) Part of the Laue pattern of a single HEWL recorded with the MAR345 detector. Nine spots circled (in red online) are identified in terms of number of Miller indices. Spot positions are represented with a (red online) circle on the image of the same diffraction pattern acquired with the XPAD3S-Si (*b*) and the XPAD3S-CdTe (*c*) with identical exposure time. Images (*b*) and (*c*) are displayed with the same intensity scale.

using the *LAUEGEN* software (Campbell, 1995). The resulting diffraction spots, classified *via* the orientation matrix, were visually identified on the XPAD3-CdTe and XPAD3-Si detectors calibrated as described in §2.2. Fig. 8 shows part of the diffraction pattern measured with the MAR345, XPAD3-Si and XPAD3-CdTe detectors.

As a proof of the method, eight well separated spots, circled in red in Fig. 8, were chosen and their predicted energies (given at the position of the maximum intensity) and multiplicity are listed in Table 2. The superior quantum efficiency of the CdTe detector at high energy is visually illustrated by the high-energy reflection [8 6 1] which is clearly visible on the CdTe image (Fig. 8*c*) but not on the Si image (Fig. 8*b*). The maximum count rate recorded on each detector was inferior to 3000 photons s^{-1} $pixel^{-1}$.

In order to perform the incident photon energy measurement with the pixel detectors, a curve of the measured counts, as a function of ITH then converted to energy by using the calibration detailed in §2.2.2, was extracted from the most intense pixel of each spot. In order to suppress the diffuse X-ray background, the counting curve of a pixel located outside the spot and close to the most intense pixel was subtracted from the above signal. Fig. 9(*a*) presents the corrected curves measured on the spot [5 2 0] with the XPAD3S-Si and XPAD3S-CdTe. As expected, compared with the Si detector, better statistics are obtained with the CdTe above 15 keV. Incident energy is extracted by fitting the data with a sum of functions (2), and hence allowing the characterization of multiplet components. The spectrum is obtained by differentiation of the fit (*cf.* Fig. 9*b*). Energy reconstruction of the eight spots measured with the CdTe detector is compared with the predicted energies in Table 2 and a good agreement is obtained. Several other diffraction spots were measured, but their energy calibration impaired as they fell across junctions between detector modules. Nothwithstanding, the correct multiplet assignment was clear for these reflections even when the energy calibration was noisy, indicating their potential usefulness in future fitting of the orientation matrix.

The energy resolution of the CdTe detector also allowed direct measurement of the energy variation within a spot along the Bragg angle resulting from the beam polychromaticity. This variation is shown in Fig. 10 for the [5 2 0] reflection.

4. Conclusion

This experiment clearly demonstrates that the calibration procedures applied to the energy dispersion of the XPAD3 detectors are sufficiently accurate for us to measure diffused or diffracted X-rays at different energies and with good energy resolution. This enabled us to separate reflections which, with a non-energy-resolving detector, are superposed using the Laue method and, consequently, gives us the possibility of 'filling' the 'low-resolution hole' with measured data. The low number of spots that we were able to measure on the limited surface area of the CdTe detector is insufficient to scale reflections or to make statistically significant comparisons with

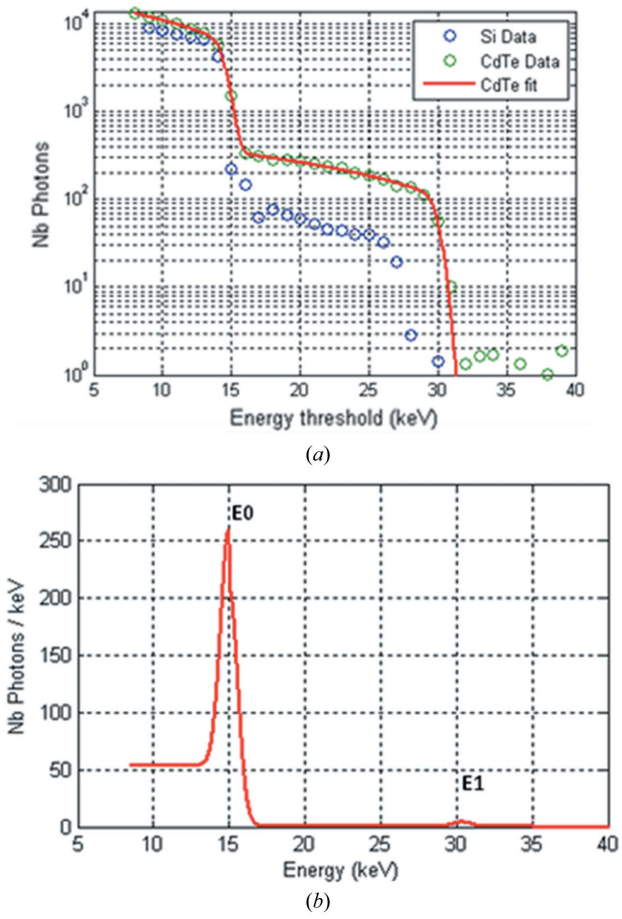

Figure 9
(*a*) Plot of intensity *versus* energy of the [5 2 0] reflection measured on the XPAD3S-CdTe and on the XPAD3S-Si. XPAD3S-CdTe data are fitted with a sum of two functions (2) (red curve). (*b*) Spectrum obtained by differentiation of the fit. The fundamental (E_0) and first harmonic (E_1) are identified.

refined structure factors available in the Protein Data Bank; this investigation is the subject of further measurements in progress at SOLEIL. The expected signal-to-noise ratio of such a spot integration can be judged by inspection of Fig. 9(*b*), which is equivalent to the measured intensities for a single pixel.

A number of applications in modern MX (see, for example, Cornaby, 2010) could be addressed using this technical improvement to the Laue method. Certain measurements suffer from the constraint of limited opening angle [for example, owing to use of diamond anvil cells in high-pressure crystallography; such an application has been discussed by Ice *et al.* (2005)] or difficulty in orienting the crystal (for example, with *in situ* crystal plate screening, where a crystallization plate is translated and reoriented in an X-ray beam to identify crystal 'hits', or for room-temperature data collection in micro-fluidic or capillary media). The additional completeness of data with limited sample rotation range afforded by using white-beam methods could be a significant advantage in this context, and considerably simpler and cheaper than using robotic goniometry.

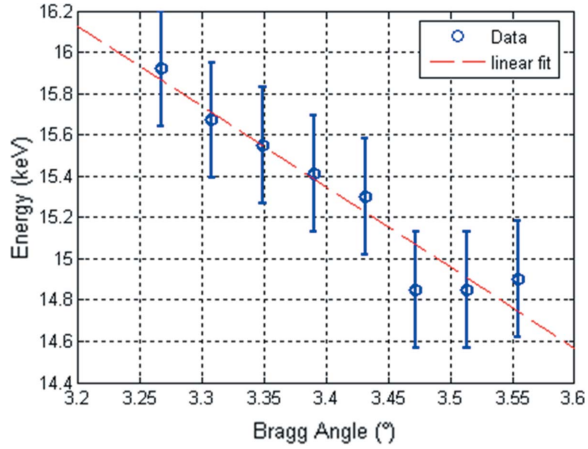

Figure 10
Energy variation within the [5 2 0] reflection along the 2θ angle with a 2σ error bar (2×140 eV). The data are fitted with a linear function.

Furthermore, the good DQE of the CdTe pixel detector at high energies and its high signal-to-noise ratio even at low count rate (owing to photon counting and negligible detector noise) make it an outstanding tool for exploiting the gain of data collection efficiency in MX when using higher-energy photons reported by Fourme *et al.* (2011), or for overcoming the relatively high absorption of crystallization media. Notwithstanding, beyond this proof of principle, a number of technical problems remain to be solved.

First and foremost, the size of the current CdTe detector is a limitation. In addition, the relationship between the size of a detector and the dead area on the surface of the detector (inter-module distances) becomes more complicated when the detector is intended to function at high energies as reciprocal space is more densely sampled. Furthermore the 'stretching' of Laue diffraction spots owing to the polychromatic beam increases the likelihood of spatially overlapping reflections and hence implies much large detector surfaces. Raster scanning a smaller detector to give a larger detector surface is, of course, possible, but raises the objection that data collection would be very inefficient in terms of X-ray dose per measured diffraction spot. An extreme example of such a situation was encountered by the authors during these measurements (data not presented), where a crystal of thaumatin 'died' during the collection of such a tiled image (the earlier images showing significantly higher resolution diffraction than the later images).

Secondly, the incoming X-ray bandpass was constant during the whole experiment, so that radiation damage ensued from the whole energy spectrum, whereas a smaller part of the energy spectrum was measured. This unsatisfactory state of affairs could be improved by using a broad bandpass monochromatic beam whose energy is incremented along with the detector window. This latter experiment would be equivalent to scanning the energy spectrum exciting the crystal and using a non-energy-resolving detector, but with several advantages. Firstly, mechanical scanning of the energy range of a beamline is not straightforward, can be slow and is subject to careful calibration (to take into account changes to bandpass, beam

divergence or polarization with energy). On the other hand, the scanning of the threshold of a PAD detector is rapid, has only a weak dependence of point spread function *versus* energy as compared with, for example, a CCD detector, the low energy cut-off of the measured energy spectrum is 'clean', and the method maintains all the advantages of a PAD in terms of signal to noise combined with high dynamic range. A further and not insignificant point is the possibility to discriminate between fluorescence (for example, resulting from an anomalous diffuser in the crystallization buffer) and diffraction, which is not possible with an integrating detector. It must be noted, however, that developments in detector technology may change the balance of these advantages in the future.

Notwithstanding the drawbacks of this type of approach, the possibility of collecting h, k, l, F and E at the same time promises to open up new possibilities for MX data collection and the development of new analysis techniques to make use of the energy in indexing and integration of data.

The authors would like to thank the XPIX collaboration for the development of the detector and their help in developing new functionality, and Synchrotron SOLEIL and in particular the METROLOGIE beamline for data collection. AT would like to thank Professor J. Helliwell, Manchester University, for helpful discussions and encouragement.

References

Basolo, S., Berar, J. F., Boudet, N., Breugnon, P., Chantepie, B., Clemens, J. C., Delpierre, P., Dinkespiler, B., Hustache, S., Medjoubi, K., Menouni, M., Morel, Ch., Pangaud, P. & Vigeolas, E. (2008). *Nucl. Instrum. Methods Phys. Res. A*, **589**, 268–274.

Bergamaschi, A., Cervellino, A., Dinapoli, R., Gozzo, F., Henrich, B., Johnson, I., Kraft, P., Mozzanica, A., Schmitt, B. & Shi, X. (2010). *J. Synchrotron Rad.* **17**, 653–668.

Bourenkov, G. P., Popov, A. N. & Bartunik, H. D. (1996). *Acta Cryst.* A**52**, 797–811.

Campbell, J. W. (1995). *J. Appl. Cryst.* **28**, 228–236.

Chantepie, B. (2008). PhD thesis, Université de la Méditerranée Aix-Marseille II, France.

Cornaby, S., Szebenyi, D. M. E., Smilgies, D.-M., Schuller, D. J., Gillilan, R., Hao, Q. & Bilderback, D. H. (2010). *Acta Cryst.* D**66**, 2–11.

Cruickshank, D. W. J., Helliwell, J. R. & Moffat, K. (1987). *Acta Cryst.* A**43**, 656–674.

Dawiec, A. (2011). PhD thesis, Université de la Méditerranée Aix-Marseille II, France.

Delpierre, P., Basolo, S., Berar, J. F., Bordessoule, M., Boudet, N., Breugnon, P., Caillot, B., Chantepie, B., Clemens, J. C., Dinkespiler, B., Hustache-Ottini, S., Meessen, C., Menouni, M., Morel, C., Mouget, C., Pangaud, P., Potheau, R. & Vigeolas, E. (2007). *Nucl. Instrum. Methods Phys. Res. A*, **572**, 250–253.

Fourme, R., Girard, E., Dhaussy, A.-C., Medjoubi, K., Prangé, T., Ascone, I., Mezouar, M. & Kahn, R. (2011). *J. Synchrotron Rad.* **18**, 31–36.

Friedrich, W., Knipping, P. & Laue, M. (1912). *Sitzungsber. K. Bayer. Akad. Wiss. Muenchen*, pp. 303–322.

Hanley, Q. S., Campbell, J. W. & Denton, M. B. (1997). *J. Synchrotron Rad.* **4**, 214–222.

Hao, Q., Harding, M. M. & Campbell, J. W. (1995). *J. Synchrotron Rad.* **2**, 27–30.

Helliwell, J. R., Habash, J., Cruickshank, D. W. J., Harding, M. M., Greenhough, T. J., Campbell, J. W., Clifton, I. J., Elder, M., Machin, P. A., Papiz, M. Z. & Zurek, S. (1989). *J. Appl. Cryst.* **22**, 483–497.

Henrich, B., Bergamaschi, A., Broennimann, C., Dinapoli, R., Eikenberry, E. F., Johnson, I., Kobas, M., Kraft, P., Mozzanica, A. & Schmitt, B. (2009). *Nucl. Instrum. Methods Phys. Res. A*, **607**, 247–249.

Ice, G. E., Dera, P., Liu, W. & Mao, H.-k. (2005). *J. Synchrotron Rad.* **12**, 608–617.

Idir, M., Mercere, P., Moreno, T., Delmotte, A., Dasilva, P. & Modi, M. H. (2010). *AIP Conf. Proc.* **1234**, 485–488.

Marchal, J. (2010). *J. Instrum.* **5**, P01004.

Medjoubi, K., Bucaille, T., Hustache, S., Bérar, J.-F., Boudet, N., Clemens, J.-C., Delpierre, P. & Dinkespiler, B. (2010). *J. Synchrotron Rad.* **17**, 486–495.

Medjoubi, K., Hustache, S., Picca, F., Bérar, J. F., Boudet, N., Bompard, F., Breugnon, P., Clémens, J. C., Dawiec, A., Delpierre, P., Dinkespiler, B., Godiot, S., Logier, J. P., Menouni, M., Morel, C., Nicolas, M., Pangaud, P. & Vigeolas, E. (2011). *J. Instrum.* **6**, C01080.

Moffat, K. (1997). *Methods Enzymol.* **277**, 433–447.

Pangaud, P., Basolo, S., Boudet, N., Berar, J. F., Chantepie, B., Clemens, J. C., Delpierre, P., Dinkespiler, B., Medjoubi, K., Hustache, S., Menouni, M. & Morel, Ch. (2008). *Nucl. Instrum. Methods Phys. Res. A*, **591**, 159–162.

Pangaud, P., Basolo, S., Boudet, N., Berar, J. F., Chantepie, B., Delpierre, P., Dinkespiler, B., Hustache, S., Menouni, M. & Morel, C. (2007). *Nucl. Instrum. Methods Phys. Res. A*, **572**, 321–324.

Ponchut, C. (2008). *Nucl. Instrum. Methods Phys. Res. A*, **591**, 311–313.

Radeka, V. (1988). *Ann. Rev. Nucl. Part. Sci.* **38**, 217–277.

Ren, Z. & Moffat, K. (1995). *J. Appl. Cryst.* **28**, 482–494.

Rossi, G., Renzi, M., Eikenberry, E. F., Tate, M. W., Bilderback, D., Fontes, E., Wixted, R., Barna, S. & Gruner, S. M. (1999). *J. Synchrotron Rad.* **6**, 1096–1105.

Sanchez del Rio, M. & Dejus, R. J. (2004). *Proc. SPIE*, **5536**, 171–174.

Send, S., von Kozierowski, M., Panzner, T., Gorfman, S., Nurdan, K., Walenta, A. H., Pietsch, U., Leitenberger, W., Hartmann, R. & Strüder, L. (2009). *J. Appl. Cryst.* **42**, 1139–1146.

Spieler, H. (2008). *Semiconductor Detector Systems.* Oxford: Oxford Science Publications.

Šrajer, V., Crosson, S., Schmidt, M., Key, J., Schotte, F., Anderson, S., Perman, B., Ren, Z., Teng, T., Bourgeois, D., Wulff, M. & Moffat, K. (2000). *J. Synchrotron Rad.* **7**, 236–244.

Toyama, H., Higa, A., Yamazato, M., Maehama, T., Ohno, R. & Toguchi, M. (2006). *Jpn. J. Appl. Phys.* **45**, 8842–8847.

Toyokawa, H., Kajiwara, K. & Sato, M. (2010). *Nuclear Science Symposium Conference Record (NSS/MIC) IEEE*, 30 October–6 November 2010, pp. 333–335.